Aerosol optical depth thresholds as a tool to assess diffuse radiation fertilization of the land carbon uptake in China

Xu Yue[1] and Nadine Unger[2]

[1] Climate Change Research Center, Institute of Atmospheric Physics, Chinese Academy of Sciences, Beijing 100029, China

[2] College of Engineering, Mathematics and Physical Sciences, University of Exeter, Exeter, EX4 4QE, UK

Correspondence to: X. Yue (yuexu@mail.iap.ac.cn)

15   **Abstract**

17   China suffers from frequent haze pollution episodes that alter the surface solar radiation and

18   influence regional carbon uptake by the land biosphere. Here, we apply combined vegetation

19   and radiation modeling and multiple observational datasets to assess the radiative effects of

20   aerosol pollution in China on the regional land carbon uptake for the 2009-2011 period. First,

21   we assess the inherent sensitivity of China's land biosphere to aerosol pollution by defining

22   and calculating two aerosol optical depth (AOD) at 550 nm thresholds (i) AOD_{t1}, resulting in

23   the maximum net primary productivity (NPP), and (ii) AOD_{t2}, such that if local AOD <

24   AOD_{t2}, the aerosol diffuse fertilization effect (DFE) always promotes local NPP compared

25   with aerosol-free conditions. Then, we apply the thresholds, satellite data, and interactive

26   vegetation modeling to estimate current impacts of aerosol pollution on land ecosystems. In

27   the Northeast, observed AOD is 55% lower than AOD_{t1}, indicating strong aerosol DFE on

28   local NPP. In the southeastern coastal regions, observed AOD is close to AOD_{t1}, suggesting

29   that regional NPP is promoted by the current level of aerosol loading but that further

30   increases in AOD in this region will weaken the fertilization effects. The North China Plain

31   experiences limited enhancement of NPP by aerosols because observed AOD is 77% higher

32   than AOD_{t1} but 14% lower than AOD_{t2}. Aerosols always inhibit regional NPP in the

33   Southwest because of the persistent high cloud coverage that already substantially reduces

34   the total light availability there. Under clear-sky conditions, simulated NPP shows

35   widespread increases of 20-60% (35.0 ± 0.9 % on average) by aerosols. Under all-sky

36   conditions, aerosol pollution has spatially contrasting opposite sign effects on NPP from -3%

37   to +6% (1.6 ± 0.5% on average), depending on the local AOD relative to the regional

38   thresholds. Stringent aerosol pollution reductions motivated by public health concerns,

39   especially in the North China Plain and the Southwest, will help protect land ecosystem

40   functioning in China and mitigate long-term global warming.

41

42

1 Introduction

Atmospheric aerosols scatter and absorb solar radiation, while plants rely on sunlight for photosynthesis. Thus, aerosols affect land carbon uptake through radiative perturbations. In particular, observations have demonstrated that aerosols can enhance canopy photosynthesis and light-use efficiency (LUE = GPP/PAR, GPP is gross primary productivity and PAR is photosynthetically active radiation) by increasing diffuse radiation in the lower canopy (Gu et al., 2003; Rap et al., 2015; Strada et al., 2015). This aerosol diffuse fertilization effect (DFE) is subject to the aerosol loading and sky conditions (Cohan et al., 2002; Oliphant et al., 2011) because the potential benefit of increased diffuse radiation in the lower canopy can be offset or even reversed by the concomitant reductions in direct sunlight. China is the world largest anthropogenic emitter of carbon dioxide reaching 2.5 Pg C yr^{-1} (Liu et al., 2015), while the land ecosystems mitigate only around 0.2 Pg C yr^{-1} with large uncertainties (Piao et al., 2009). At the same time, China encounters frequent haze pollution events due to large emissions of anthropogenic aerosols and precursors (Guo et al., 2014; Wang and Chen, 2016). It is critically important to understand how this haze pollution affects the land carbon sink in China.

Leaf photosynthesis increases with the solar irradiance before reaching saturation (Farquhar et al., 1980). For a canopy with complex composition and vertical distribution, only sunlit leaves receive both direct and diffuse sunlight. Typically, irradiance is abundant for these leaves and photosynthesis is light saturated. In contrast, shaded leaves receive only diffuse radiation and their photosynthesis is usually light-limited (He et al., 2013). Existence of aerosol pollution and/or a cloud layer simultaneously increases diffuse radiation but decreases direct radiation. The enhancement of diffuse radiation helps increase photosynthesis by the shaded leaves but the response of the sunlit leaves depends on the level of aerosol/cloud loading. Moderate reductions of direct sunlight will not decrease photosynthesis of sunlit leaves because the light availability is still saturated. Consequently, the GPP of the whole canopy (sunlit plus shaded portions) increases due to the improved LUE (Knohl and Baldocchi, 2008). Large reductions of direct sunlight may convert the light-saturated regime to light-limited regime for the sunlit leaves, leading to reduced LUE and dampened canopy GPP (Alton, 2008). Photosynthetic response to diffuse light is also dependent on plant functional type (PFT). C4 plants are less sensitive to the enhanced diffuse radiation compared to C3 plants because C4 plants do not become light saturated under high irradiance. As a result C4 plants are more sensitive to the reductions in direct light than C3

plants (Kanniah et al., 2012). Thus, the net effect of aerosol pollution on canopy carbon uptake depends on the aerosol loading, cloud amount, geographic location, and the plant species.

Previous observation-based studies of cloud and aerosol DFE are summarized in Table 1. Most observational studies have detected DFE using long-term ground-based measurements (Niyogi et al., 2004; Cirino et al., 2014). Currently, direct measurements of DFE on photosynthesis in China are limited (Li et al., 2014). Observations suggest that both clouds and aerosols exert similar impacts on land carbon uptake (Kanniah et al., 2012). Many observational studies have found that canopy GPP of trees maximizes with diffuse fraction (DF) of 0.4-0.7 (Rocha et al., 2004; Alton, 2008). For grass and savanna, the optimal DF is as low as 0.2-0.3, above which the carbon uptake will decrease (Alton, 2008; Kanniah et al., 2013). The appearance of thin cloud may enhance net ecosystem productivity (NEP) of trees by 7-11% (Monson et al., 2002; Misson et al., 2005), while thick cloud reduces carbon uptake due to large irradiance attenuation (Rocha et al., 2004; Cheng et al., 2016). Aerosol light scattering in clear sky may increase NEP of trees by 8-29% (Misson et al., 2005; Cirino et al., 2014), but decreases the carbon uptake of grassland (Niyogi et al., 2004). Previous vegetation modeling results are generally consistent with observations (Table 1). For example, Knohl and Baldocchi (2008) predicted maximum GPP with DF of 0.45 for a deciduous forest.

In this study, we apply the **Y**ale **I**nteractive terrestrial **Bio**sphere (YIBs) model (Yue and Unger, 2015) combined with the **C**olumn **R**adiation **M**odel (CRM) to analyze the impacts of aerosol DFE on net primary productivity (NPP) in China in the present day world. The main objective is to explore the responses of NPP to current aerosol pollution with and without the appearance of clouds. First, we perform multiple sensitivity experiments to derive the NPP sensitivity to aerosol optical depth (AOD) at 550 nm and compare it with available observations (Table 1). Second, we calculate the aerosol-induced DFE 'tolerance' of China's land biosphere by defining and computing two thresholds of AOD: (i) AOD_{t1}, resulting in the maximum NPP, and (ii) AOD_{t2}, such that if local AOD < AOD_{t2}, the aerosol DFE always promotes local NPP compared with aerosol-free conditions. Third, we estimate changes in NPP between simulations with and without aerosol DFE, and relate these changes to the derived AOD thresholds so as to understand the causes of NPP responses to aerosol radiative effects. Our model approach offers a large regional scale assessment, and is not limited by spatiotemporal and species-specific sampling issues (Table 1). We consider aerosol-induced perturbations to diffuse, direct, and total PAR under both clear and cloudy sky conditions, but ignore the meteorological and hydrological feedbacks from those perturbations. Section 2

describes the measurement data, vegetation and radiation models, and the full group of simulations. Section 3 presents the model evaluation, the sensitivity of GPP to aerosol pollution in China, the derived AOD thresholds, and the simulated NPP responses to current levels of aerosol pollution. Section 4 summarizes and discusses the main results.

2 Methods

2.1 The Yale Interactive Terrestrial Biosphere Model (YIBs)

The YIBs is a process-based vegetation model that simulates global terrestrial carbon cycle with dynamic predictions of leaf area index (LAI) and tree growth (Yue and Unger, 2015). Plant photosynthesis is simulated using the well-established Farquhar scheme (Farquhar et al., 1980) and is coupled to stomatal conductance with the Ball-Berry scheme (Ball et al., 1987). The canopy radiative transfer scheme separates diffuse and direct PAR for sunlit and shaded leaves (Spitters, 1986), depending on solar zenith angle and canopy LAI (section 2.3). Autotrophic respiration (Ra) is split into maintenance and growth components, and is dependent on leaf temperature and nitrogen content (Clark et al., 2011). The model includes 9 PFTs, including evergreen needleleaf forest (ENF), deciduous broadleaf forest (DBF), evergreen broadleaf forest (EBF), shrubland, tundra, C3/C4 grassland, and C3/C4 cropland (Fig. S1). This land cover is derived based on retrievals from both MODIS (Hansen et al., 2003) and the Advanced Very High Resolution Radiometer (AVHRR) (Defries et al., 2000). The fraction of C4 cropland is derived based on the total crop fraction and the ratio of C4 species (Monfreda et al., 2008).

The YIBs can be used in three different configurations: site-level, global/regional offline, and online within a climate model. For this study, we use the regional offline version driven with hourly 1°×1° meteorological forcings from the NASA Modern Era Retrospective-analysis for Research and Applications (MERRA). On the global scale, simulated LAI, tree height, phenology, GPP, and NPP show reasonable spatial distribution and long-term trends compared with both *in situ* measurements and satellite retrievals (Yue and Unger, 2015; Yue et al., 2015a; Yue et al., 2015b). Other carbon fluxes such as NEP, autotrophic respiration, and heterotrophic respiration are also reasonably simulated relative to multiple model ensembles (Yue et al., 2015b).

2.2 The Column Radiation Model (CRM)

The CRM is the standalone version of the radiation model used by the NCAR Community Climate Model, which has been updated to the Community Earth System Model (http://www.cesm.ucar.edu/models/). Using temporal-varying aerosol profiles (types and concentrations) and meteorological reanalyses, the CRM model calculates reflectivity and transmission of atmospheric layers, emissivity and absorptivity of greenhouse gases (GHGs), and Mie scattering and absorption of aerosols. Aerosol optical parameters associated with each aerosol species, including specific extinction coefficients, single scattering albedo, and asymmetric parameters, are adopted from Yue et al. (2010) for mineral dust, Yue and Liao (2012) for sea salt, and RegCM4 model for other species (Giorgi et al., 2012). These parameters vary with changes in both wavelength and relative humidity (Fig. S2). Sulfate and nitrate aerosols share the same parameters. For carbonaceous aerosols (black carbon (BC) and organic carbon (OC)), half are considered hydrophobic and half are hydrophilic.

The CRM is driven with hourly 1°×1° fields of temperature, humidity, and [O3] at 20 sigma levels interpolated from the MERRA data. Vertical profiles of cloud cover and liquid water path are adopted from the CERES SYN1deg (http://ceres.larc.nasa.gov), which are determined using remote sensing from MODIS and the Visible and Infrared Sounder (VIRS). Surface albedo, temperature, and pressure are also adopted from MERRA. The CRM model utilizes aerosol profile of all species simulated by the ModelE2-YIBs, a fully coupled chemistry-carbon-climate model (Schmidt et al., 2014). Aerosol components include sulfate, nitrate, BC, OC, dust (clay and silt), and sea salt (accumulation and coarse modes). Concentrations of these pollution species are predicted based on emission inventories of the year 2010 from the Greenhouse Gas and Air Pollution Interactions and Synergies (GAINS) integrated assessment model (Amann et al., 2011). We compare the GAINS v4a inventory with the HTAP inventory adopted from the Emissions Database for Global Atmospheric Research (EDGAR, http://edgar.jrc.ec.europa.eu) and RCP8.5 inventory from the Intergovernmental Panel on Climate Change (IPCC, http://www.ipcc.ch/) (Fig. S3). The inter-comparison shows that the GAINS has similar magnitude (differences within ±10%) of emissions for major pollutants over China as HTAP and RCP8.5, except for ammonia, which is higher by 50-80% in GAINS. Simulated summertime surface PM2.5 concentrations show high correlations (*R*=0.76) and low biases (NMB=1.6%) with *in situ* measurements at 188 sites (not shown).

2.3 Canopy radiative transfer and carbon uptake

178 We use the multilayer canopy radiative transfer scheme proposed by Spitters (1986) to
179 separate diffuse and direct PAR for sunlit and shaded leaves. The canopy is divided into an
180 adaptive number of layers (typically 2-16) for light stratification. Light intensity decreases
181 exponentially with LAI when penetrating in the canopy:

182
$$I = (1-\rho) \cdot I_t \cdot e^{-kL} \qquad (1)$$

183 where I_t is the total PAR at the top of canopy, L is the LAI from the top of canopy to layer n,
184 I is the total PAR available for absorption at the depth L, and k is the extinction coefficient.
185 Here, ρ is the reflection coefficient calculated as follows:

186
$$\rho = \left(\frac{1-(1-\sigma)^{1/2}}{1+(1-\sigma)^{1/2}}\right)\left(\frac{2}{1+1.6\cos\alpha}\right) \qquad (2)$$

187 where α is the solar zenith, $\sigma = 0.2$ is the scattering coefficient of single leaves. Light
188 absorption at the depth L is estimated as follows:

189
$$I_a = -dI/dL = (1-\rho) \cdot I_t \cdot k \cdot e^{-kL} \qquad (3)$$

190 where I_a is the flux absorbed per unit leaf area. The total PAR at the top of canopy is consist
191 of diffuse (I_{tf}) and direct (I_{tr}) components, both of which are simulated with CRM model:

192
$$I_t = I_{tf} + I_{tr} \qquad (4)$$

193 According to equation (3), absorption of the diffuse flux is calculated as:

194
$$I_{fa} = (1-\rho) \cdot I_{tf} \cdot k_f \cdot e^{-k_f L} \qquad (5)$$

195 where $k_f = 0.8(1-\sigma)^{1/2}$ is the extinction coefficient of the diffuse flux. For the direct flux, it is
196 segregated into diffuse and direct components on its way through the canopy. The total
197 absorption of direct flux is calculated as:

198
$$I_{ra} = (1-\rho) \cdot I_{tr} \cdot (1-\sigma)^{1/2} \cdot k_r \cdot e^{-(1-\sigma)^{1/2}k_r L} \qquad (6)$$

199 where $k_r = 0.5/\cos\alpha$ is the extinction coefficient of direct component of the direct flux. Here
200 the function $(1-\sigma)^{1/2}$ is applied to account for the scattering effects of leaves for direct light.
201 The absorption of the direct component of direct flux is calculated as:

202
$$I_{rra} = (1-\sigma) \cdot I_{tr} \cdot k_r \cdot e^{-(1-\sigma)^{1/2}k_r L} \qquad (7)$$

203 We distinguish light absorption for shaded and sunlit leaves. Shaded leaves absorb diffuse
204 flux and the diffuse component of direct flux:

205
$$I_{sha} = I_{fa} + (I_{ra} - I_{rra}) \qquad (8)$$

206 Sunlit leaves absorb both diffuse and direct radiation:

207
$$I_{sla} = I_{sha} + (1-\sigma) \cdot k_r \cdot I_{tr} \qquad (9)$$

208 Photosynthesis is calculated separately for shaded and sunlit leaves based on the different
209 light absorption. Canopy photosynthesis (μmol C s^{-1} per unit leaf area) is the sum of these
210 two parts of leaves:

211 $$A = f_{sl} \cdot A_{sl} + (1 - f_{sl}) \cdot A_{sh} \tag{10}$$

212 where A_{sl} and A_{sh} are photosynthesis of sunlit and shaded leaves, respectively. The fraction of
213 sunlit leaf area f_{sl} is calculated as:

214 $$f_{sl} = e^{-k_r L} \tag{11}$$

215 Finally, the total carbon uptake GPP (μmol C s^{-1} per unit ground area) is estimated as follows:

216 $$GPP = \int_0^{LAI} A \cdot dL \tag{12}$$

217

218 **2.4 Simulations**

219 We conduct simulations combining the offline YIBs vegetation model and the CRM radiation
220 model. Diffuse and direct PAR at the top of canopy is predicted with CRM model. These
221 radiative fluxes are then used as input for the YIBs model, which further separates diffuse
222 and direct fluxes absorbed by sunlit and shaded leaves using Spitters (1986) canopy scheme.
223 We perform two groups of YIBs-CRM sensitivity simulations, 30 for clear-sky conditions
224 and 30 for all-sky conditions, to derive the AOD thresholds for aerosol DFE (Table 2). The
225 YIBs model is driven with meteorological forcings from MERRA, except for direct and
226 diffuse PAR, which is predicted with the CRM model. We set up baseline simulations
227 (CLR010 and ALL010) with the aerosol profile from ModelE2-YIBs and validated optical
228 parameters. In other simulations, specific scaling factors ranging from 0.0 to 30 are applied to
229 aerosol concentrations to represent variations of AOD. Due to the disk storage limit for
230 hourly meteorological profiles, we perform CRM simulations for 2009-2011. The simulated
231 PAR is alternately applied as input for the YIBs model, which uses additional meteorological
232 forcings from MERRA for 2000-2011. In this case, predicted PAR at 2009-2011 is recycled
233 as input for periods of 2000-2002, 2003-2005, 2006-2008, and 2009-2011 in the YIBs
234 simulations. The last 3 years of YIBs output, including GPP and NPP, are used for analyses.
235 We focus our analyses for the summer (June-July-August) season, when both AOD and
236 carbon fluxes are high.

237

238 **2.5 Benchmark and evaluation observational datasets**

239 To evaluate GPP simulated with the YIBs model, we use global benchmark product upscaled

240 from the FLUXNET eddy covariance data for 2009-2011 (Jung et al., 2009). For NPP, we

241 use the satellite product of 2009-2011 retrieved by the Moderate Resolution Imaging

242 Spectroradiometer (MODIS) (Zhao et al., 2005). The MODIS dataset provides indirect

243 estimates of global NPP using an empirical light-use function between GPP and meteorology,

244 as well as the modeled plant respiration. The actual values of MODIS NPP may exhibit

245 certain biases at the regional scale compared with site-level observations (Pan et al., 2006).

246 However, the spatial pattern of the product is in general reasonable and has been widely used

247 for model evaluations (e.g., Collins et al., 2011; Pavlick et al., 2013). To evaluate surface

248 radiative fluxes simulated with the CRM model, we use ground-based radiation data for

249 2008-2012 from 106 pyranometer sites in China, provided by the Climate Data Center,

250 Chinese Meteorological Administration (Xia, 2010). For each site and each month, we derive

251 the monthly mean radiative fluxes based on daily data if <30% days are missing. We then

252 select sites where all months are available for 2008-2012, leaving a total of 95 sites for the

253 evaluation of total shortwave radiation. Diffuse radiation is not observed at all sites, and only

254 a total of 17 sites meet the criteria for the continuous measurements. For aerosol radiative

255 effects, we use assimilation data of surface radiative fluxes adopted from the SYN1deg

256 product of NASA Clouds and the Earth's Radiant Energy System (CERES) (Wielicki et al.,

257 1996; Rutan et al., 2015). Aerosol effect in CERES is calculated with the Langley Fu-Liou

258 radiative transfer model (Fu and Liou, 1993), using aerosol profiles simulated by the Model

259 for Atmospheric Transport and Chemistry (Rasch et al., 1997). We also use satellite-based

260 AOD data of MOD08_M3 for 2008-2012 retrieved by MODIS onboard the Terra platform

261 (Remer et al., 2005). All gridded data are interpolated onto 1°×1° grids, matching the

262 resolution of both CRM and YIBs models.

263

264

265 **3 Results**

266

267 **3.1 Model evaluation**

268   The YIBs model predicts reasonable spatial distribution of carbon fluxes compared with

269 other data products (Fig. 1). For the summer, high GPP and NPP is simulated in the Northeast,

270 Southwest, and southeastern coastal regions, where DBF and ENF trees dominate (Fig. S1).

271 The correlation coefficients between simulations and proxy data are as high as 0.8 for both

272 GPP and NPP. Predicted GPP is -24% lower on average than benchmark product, mainly

273   because the model shows smaller values over North China Plain. The normalized mean bias

274   (NMB) of NPP is close to 0, because of the regional offsetting. On the annual mean basis,

275   simulations show higher correlations ($R = 0.84$ for GPP and 0.86 for NPP) and similar NMB

276   (-21% for GPP and -16% for NPP) compared with data products.

277   The CRM predicts opposite spatial distribution for total solar radiation and the

278   corresponding DF (Fig. 2). For radiation, high values are found in the North and West, while

279   low values in the East and Southwest. Such pattern is related to cloud cover, which is lower

280   in the north but higher in the south, especially the Southwest where cloud cover is usually

281   higher than 80% (Fig. S4). Due to the cloud scattering, those regions with low insolation

282   have high DF. Compared with *in situ* measurements, the simulated total radiation exhibits

283   reasonable spatial characteristics and the correlation coefficient is as high as 0.88. The

284   evaluation of DF shows certain biases but is reasonable over the East (blue points of Fig. 2f),

285   which is the major domain for this study.

286   The CRM also predicts reasonable AOD and aerosol radiative effects (Fig. 3). Using

287   aerosol concentrations from the climate model ModelE2-YIBs, the CRM simulates high

288   regional AOD centered in the North China Plain. Previous sensitivity tests with ModelE2-

289   YIBs shows that such high loading of aerosols is mainly (>80%) contributed by

290   anthropogenic emissions. The AOD is generally high over the vast domain of eastern China

291   but low in the western part. Compared with AOD from CERES, which is derived using

292   aerosol concentrations from a chemical transport model, the AOD in CRM presents

293   reasonable spatial distribution with high correlation coefficient of 0.7 and low NMB of -1%.

294   However, compared with MODIS AOD, which is derived based on satellite retrievals, the

295   predicted AOD is on average overestimated by 30% in eastern China. For the following

296   analyses, we use the predicted AOD as the benchmark but discuss the influence of its

297   overestimation on the predicted aerosol DFE. We further assess aerosol radiative efficiency

298   (ARE), defined as radiative forcing per unit AOD, over China. Higher magnitude of ARE is

299   predicted in the North and West, because lower cloud coverage there allows larger radiative

300   perturbations by the same level of aerosols. The comparison of ARE between CRM and

301   CERES shows high correlation coefficient of 0.87. However, ARE in CRM is smaller by 21%

302   in magnitude than that in CERES.

303

304   **3.2 Sensitivity of GPP to DF and AOD in China**

305   Appearance of cloud and/or aerosols increases DF but decreases total insolation. We

306   examine PFT-specific GPP responses to DF for clear and all-sky conditions (Fig. 4). Under

clear-sky conditions, at DF < 0.55, all PFTs show increased GPP in response to increasing DF. At low DF (DF < 0.55), shaded leaves experience low light availability because diffuse radiation is limited. Meanwhile, photosynthesis of sunlit leaves is light-saturated because direct radiation is abundant. Introduction of aerosol pollution, which increases DF, to this system redistributes sunlight to the shaded light-limited leaves (without compromising the total light availability to sunlit leaves), thus increasing the LUE and GPP of the whole canopy. The derived GPP-diffuse sensitivity (ΔGPP/ΔDF, units: g C m^{-2} day^{-1} per unit change of DF with ± 95% confidence interval) is 5.4 ± 1.2 for ENF, 6.8 ± 2.1 for DBF, 5.6 ± 1.7 for shrub (tundra plus arid shrub), 2.8 ± 0.7 for C3 herbs (C3 grassland and cropland), and 2.2 ± 2.3 for C4 herbs (C4 grassland and cropland) when DF < 0.55. However, at high DF (DF > 0.55), light is no longer saturated for sunlit leaves because of the large attenuation of direct light. Further introduction of aerosols decreases photosynthesis of sunlit leaves, which may offset the carbon gains from enhanced diffuse light by shaded leaves, resulting in a net carbon loss for the whole canopy. Although large variations in GPP, denoted as error bars, exist within each bin, they do not affect the significance of the GPP-diffuse responses. We select the GPP-diffuse sensitivity at clear-sky conditions averaged for all PFTs as an example. The largest bin-to-bin difference in GPP is calculated as 1.9 g C m^{-2} day^{-1} between DF = 0.58 and DF = 0.12. Such GPP difference is significant at $p < 0.001$ level based on a Student T test, suggesting that GPP varies significantly when the DF change is pronounced.

Under all-sky conditions, which includes both clear and cloudy skies, DF is always higher than 0.55, because existing cloud cover has already increased the diffuse light fraction in the system. Any further increase of DF by aerosol scattering has limited or even detrimental impacts on whole canopy GPP because the associated aerosol-induced reductions in direct radiation impact photosynthesis by the sunlit leaves. GPP decreases almost linearly for all PFTs in response to increasing DF > 0.55, with GPP-diffuse sensitivity of -6.9 ± 1.4 for ENF, -10.8 ± 2.3 for DBF, -3.8 ± 1.7 for shrubland, -3.8 ± 0.8 for C3 herbs, and -10.1 ± 1.6 for C4 herbs. The GPP response to increases in DF > 0.55 is almost identical under clear-sky and all-sky conditions.

The PFT-specific GPP responses to idealized perturbations in AOD depend strongly on the sky conditions (Fig. 5). Under clear sky conditions, aerosol promotes GPP for most PFTs if AOD < 2. The maximum possible enhancement of GPP is ~40% for DBF, ENF, and C3 herbs, and can be as high as 60% for shrub. Most shrub species (especially tundra) are located in the Southwest (Fig. S1). Over that region, solar irradiance is abundant at clear days

340 (not shown), allowing more efficient scattering for a given AOD. For a given AOD, the DFE

341 of C4 herbs is the weakest amongst PFTs with a maximum possible GPP enhancement of

342 only ~10%. C4 plants usually have lower LUE than C3 plants, and as a result more easily

343 become light-limited when aerosol attenuates total irradiance (Still et al., 2009; Kanniah et al.,

344 2012). A clear turning point is found for all species. For C3 plants, aerosol scattering

345 weakens GPP when AOD > 2, because photosynthesis of the sunlit leaves starts to become

346 light-limited due to reductions in direct insolation. For C4 plants, this turning point appears

347 earlier when AOD > 1. Under all-sky conditions, atmospheric aerosol shows neutral effects

348 on GPP when AOD < 1 and detrimental negative effects when AOD > 1 for all PFTs except

349 C4 (Fig. 4). For C4 plants, any addition of aerosol to the atmospheric column decreases GPP.

350   Our estimates of GPP sensitivity to DF and AOD are reasonable compared with previous

351 studies (Table 1) as summarized below: (1) the maximum enhancement of GPP is 40% at

352 clear-sky conditions for most PFTs (Gu et al., 2003); (2) the GPP enhancement of C4 plants

353 is the least due to the lowest LUE compared with other PFTs (Still et al., 2009; Kanniah et al.,

354 2012); (3) the aerosol DFE is much stronger at clear-sky than that at all-sky conditions

355 (Cohan et al., 2002); (4) both clouds and aerosols exert similar DFE on land carbon uptake

356 (Kanniah et al., 2012; Cirino et al., 2014); and (5) the maximum GPP enhancement appears

357 when DF = 0.4-0.8 (Rocha et al., 2004; Alton, 2008; Zhang et al., 2010). Most results listed

358 in Table 1 are based on NEP, however, we evaluate the sensitivity of GPP because it is the

359 direct carbon metric affected by DFE.

360

361 **3.3 Aerosol pollution DFE in China 2009-2011**

362   We apply the idealized GPP responses in Section 3.2 to estimate the current magnitude

363 of aerosol pollution DFE under realistic background conditions by defining 2 summertime

364 AOD thresholds across China (Fig. 6). The AOD thresholds are derived based on NPP (=

365 GPP − Ra), assuming no impacts of aerosol DFE on the autotrophic respiration Ra (Knohl

366 and Baldocchi, 2008). Now, we consider NPP responses, instead of GPP, because the former

367 represents the net carbon uptake by plants after subtracting autotrophic respiration for

368 maintenance and growth. The first threshold, AOD_{t1} is defined as the AOD value with the

369 maximum ΔNPP (the uppermost point of the response curve in Fig. 5), representing the

370 saturation of DFE. The second threshold, AOD_{t2} is the cross point of the response curve at

371 zero ΔNPP. For each model grid cell, if AOD is close or equal to AOD_{t1}, the peak NPP is

372 expected. If AOD<AOD$_{t2}$, aerosol DFE always promotes local NPP relative to aerosol-free

373 conditions (AOD=0).

374   We find relatively high AOD$_{t1}$ in the Northeast and low values in the Southwest (23°-

375 35°N, 100°-105°E, box d in Fig. 6a), where average cloud cover is 80% in the summer (Fig.

376 S4). The pattern of AOD$_{t2}$ is similar to that of AOD$_{t1}$ (Fig. 6b), except for high values in the

377 North (42°-48°N, 105°-118°E), where insolation is high while average cloud fraction is less

378 than 50%. The values of the AOD thresholds are much higher for clear days; for example, the

379 average clear-sky AOD$_{t1}$ is six times the all-sky values over the East (Fig. S5). Observed

380 summer AOD in the North China Plain (32°-40°N, 113°-120°E) exceeds AOD$_{t1}$ by 77% but

381 is 14% lower than AOD$_{t2}$ (Fig. 6c), suggesting limited aerosol DFE in this region. A

382 reduction of 44% in local AOD (so that AOD = AOD$_{t1}$) leads to the largest benefit for

383 regional carbon uptake. Both AOD$_{t1}$ and AOD$_{t2}$ in the Southwest are close to 0 (Fig. 6d),

384 indicating that appearance of aerosol always inhibits regional carbon uptake there. Observed

385 AOD in the Southeastern Coast (22°-°N, 110°-122°E) is approximately equal to AOD$_{t1}$ (Fig.

386 6e) and that in the Northeast (40°-47°N, 122°-132°E) is 55% lower than AOD$_{t1}$ (Fig. 6f),

387 indicating amplified carbon uptake by aerosol enhancements there.

388   To understand the relationship between the current AOD level and DFE, we calculate

389 differences between MODIS AOD and the thresholds (Fig. 7). The pattern is quite similar for

390 annual and summer differences, except that the former is less positive than the latter. The

391 stronger dampening effect by aerosols in summer is related to the higher seasonal AOD

392 (summer mean of 0.43 versus annual mean of 0.38) and cloud amount (summer mean of 65%

393 versus annual mean of 58%). Over the Southwest, current AOD level is larger than both

394 AOD$_{t1}$ and AOD$_{t2}$, suggesting that aerosols there on average inhibit NPP and further

395 increases in AOD lead to stronger inhibition. In North China Plain, AOD exceeds AOD$_{t1}$ and

396 is close to AOD$_{t2}$, indicating that aerosol pollution there has almost neutralized impacts on

397 local NPP. For the Southeast, current AOD is lower than AOD$_{t1}$ and AOD$_{t2}$ at confined

398 regions along the coast, but is higher than AOD$_{t1}$ in the inner domain. On average, observed

399 AOD of the box domain e (Fig. 6a) is lower than AOD$_{t2}$ but close to AOD$_{t1}$ (Fig. 6e),

400 suggesting that aerosols there generally promote NPP relative to aerosol-free conditions.

401 However, the potential for stronger DFE is limited as further increases of AOD will dampen

402 NPP. For the North and Northeast, current AOD is far below AOD$_{t1}$, suggesting that

403 appearance of aerosols there boosts carbon uptake, and increases in AOD continue to

404 increase NPP.

405   We calculate perturbations in NPP for different sky conditions (Fig. 8), resulting from

406   the aerosol-induced perturbations in both direct and diffuse radiation (Fig. S6). Under clear

407   sky conditions, aerosol DFE causes widespread enhancement of NPP (Fig. 8a), ranging from

408   20% to 60% over the East (Fig. S7). The absolute changes in NPP are small over North China

409   Plain (Fig. 8a), where high AOD is observed (Fig. 3). In contrast, fractional changes in NPP

410   exhibit a high center of >60% in North China Plain, consistent with the conclusion of

411   sensitivity tests that aerosols usually promote carbon uptake at clear sky (Fig. 5). Such

412   discrepancy originates from the low background (aerosol-free) NPP in North China Plain,

413   because the YIBs model applies satellite-based land cover (Fig. S1), which shows high

414   fraction of C3 cropland but almost zero tree (including ENF and DBF) coverage in North

415   China Plain. On average, aerosols increase NPP by 1.14 ± 0.01 Pg C yr^{-1} (35.0 ± 0.9 %) for

416   the whole China domain at the clear sky conditions (Fig. S7).

417   Under the all-sky conditions, aerosols drive weak patchy NPP responses (Fig. 8b),

418   mainly because of the high DF from existing cloud cover. The spatial pattern of percentage

419   NPP changes (Fig. S7b) highly resembles the AOD differences shown in Fig. 7d but with

420   opposite signs. Over the Southwest and part of North China Plain, current high level of AOD

421   exceeds AOD_{t2} and as a result inhibits local NPP by 1-2%. In the southeastern coastal regions,

422   aerosol DFE is limited, though regional AOD is below AOD_{t2}. The largest NPP enhancement

423   is predicted over the Northeast, where current AOD is far smaller than AOD_{t1} (Fig. 7c) and

424   cloud amount is moderate (Fig. S4). Regional changes of NPP range from -3% to 6% and the

425   total change is 0.07 ± 0.02 Pg C yr^{-1} (1.6 ± 0.5%) over China.

426

427   **4 Discussion and conclusions**

428

429   We provide the first assessment of aerosol pollution radiative effects on land carbon uptake

430   in China today based on regional simulations that combine the CRM radiation model and the

431   YIBs vegetation model. The confidence level of our estimate is dependent on the capability

432   of these models to reproduce observed radiative and carbon fluxes, aerosol-induced radiative

433   perturbations, and GPP responses to these perturbations. For the first two aspects, we

434   evaluate CRM and YIBs models using *in situ,* satellite, and assimilation data (Figs. 1-3). The

435   simulated GPP-AOD relationship (Figs. 4-5) is reasonable compared with available

436   measurements and modeling results in the literature (Table 1).

Our estimate is subject to limitations and uncertainties. First, calculated aerosol DFE is sensitive to the canopy radiative transfer scheme. We apply the widely used Spitters (1986) scheme to separate diffuse and direct light for sunlit and shaded leaves (2-leaf mode). This scheme invokes Beer's law that assumes light decays exponentially from the top to bottom of canopy. The predicted maximum GPP enhancement of 40% is at the high end of the range of previous modeling estimates (Table 1). A similar magnitude of GPP change was predicted by Gu et al. (2003) using different parameterizations of light partitioning and leaf photosynthesis (1-leaf mode). Mercado et al. (2009) predicted maximum GPP enhancement of only 18% for deciduous trees, considering Beer's law for light extinction and a 2-leaf model for light partitioning. Cohan et al. (2002) showed a maximum NPP enhancement of 17-30% depending on the choice of canopy scheme. These discrepancies reveal large uncertainties due to differences in the treatment of the canopy geometry (sphere or non-sphere), canopy properties (e.g., leaf clumping factor, leaf inclination angle, and leaf optical properties), light partitioning (diffuse or non-diffuse), and the upscaling of leaf photosynthesis (1-leaf or 2-leaf). More observations are required to evaluate the different parameterizations and their use in large-scale vegetation models.

Second, uncertainties in simulated AOD and aerosol radiative effects may affect the derived aerosol DFE. For this study, simulated AOD is calculated based on the three dimensional aerosol concentrations from ModelE2-YIBs climate model. Simulation shows similar spatial pattern and magnitude compared with CERES product (Figs 3a-c), which also uses aerosol profile from a chemical transport model. However, evaluations with MODIS data show that the predicted AOD is on average overestimated by 30% in eastern China (not shown). Considering that aerosol radiative efficiency from the CRM model is 21% lower than that from Fu-Liou model (Figs 3d-f), our estimate of aerosol radiative perturbations in China might be reasonable due to the offsetting biases in AOD and aerosol radiative efficiency. On the other hand, even if we ignore the uncertainties from radiative transfer scheme, the 30% overestimation in AOD does not cause large differences in the derived aerosol DFE. As a check, we calculate ΔNPP in sensitivity experiments CLR007 and ALL007 (Table 2), which employ AOD level lower by 30% than CLR010 and ALL010. We find that clear-sky ΔNPP by aerosols is 0.91 Pg C yr^{-1} (27.7%) in CLR007, lower than the enhancement of 35.0% in CLR010 (Fig. 8a). The all-sky ΔNPP by aerosols is 0.07 Pg C yr^{-1} (1.6%) in ALL007, equal to the values derived from ALL010. The reason for such similarity between ALL007 and ALL010 can be explained by the GPP-AOD relationship, which shows

470   that all-sky GPP is almost invariant when AOD<1 (Fig. 5). The results suggest that cloud

471   plays a dominant role in regulating diffuse radiation in China, and the aerosol DFE might be

472   secondary compared with cloud DFE.

473   Third, calculated aerosol DFE does not account for biotic feedbacks. Photosynthesis is

474   connected to plant physiological processes, such as stomatal conductance and respiration.

475   Observations have shown that aerosol DFE may increase water use efficiency (Rocha et al.,

476   2004; Knohl and Baldocchi, 2008), promoting plant growth and LAI that may further

477   increase canopy photosynthesis. We have assumed no responses in autotrophic respiration so

478   that the derived GPP-AOD relationship can be applied directly to NPP-AOD. Yet,

479   observations suggest that plant respiration decreases due to the aerosol-induced cooling

480   (Alton, 2008). Ignoring these biotic feedbacks indicates that NPP sensitivity to AOD

481   employed in our estimate may be underestimated.

482   Fourth, we omit the associated climatic responses to aerosol radiative effects. The

483   aerosol-induced radiative perturbations decrease surface temperature but increase relative

484   humidity (because of decreased saturation water vapor pressure) (Jing et al., 2010; Cirino et

485   al., 2014). Increases in air humidity will help enhance plant water use efficiency, leading to

486   increased photosynthesis. The impact of cooling is uncertain depending on the relationship

487   between the local background temperature and the optimal temperature of photosynthesis,

488   which is about 25°C for most species (Farquhar et al., 1980). If leaf temperature is >25°C,

489   aerosol-induced cooling is beneficial for photosynthesis. On the contrary, if leaf temperature

490   is <25°C, the cooling will act to inhibit carbon uptake. Furthermore, cloud modification,

491   caused by both aerosol direct and indirect effects, may exert complex influences on land

492   ecosystems through perturbations in diffuse radiation, surface temperature, and precipitation.

493   Resolving these concomitant biotic, meteorological, and hydrological feedbacks requires

494   earth-system models that fully couple the land biosphere, atmospheric chemistry, radiation,

495   and climate.

496   Finally, the biogeochemical response to aerosol pollution-related reactive nitrogen (N)

497   deposition is not included. Simulations with the ModelE2-YIBs climate model show that

498   anthropogenic emissions contribute 90% of the total reactive inorganic and organic N

499   deposition in China, indicating potentially large impacts of anthropogenic aerosols on

500   regional carbon uptake through the coupled C-N cycle. Using a terrestrial ecosystem model,

501   Tian et al. (2011) proposed that anthropogenic N deposition and fertilizer applications

502   together account for 61 percent of the net carbon storage in China for the 1961-2005 period.

503	The carbon sequestered per gram of deposited nitrogen decreases gradually after the year
504	1985, suggesting that most areas have reached nitrogen saturation. Similarly, based on
505	satellite retrievals, Xiao et al. (2015) revealed that anthropogenic N deposition makes no
506	significant contributions to the increases of vegetation productivity during 1982-2006.
507	Therefore, additional fertilization from aerosol N deposition may be limited because many
508	areas have been N saturated for decades such that our estimate of ΔNPP due to aerosol effects
509	based on radiative changes (Fig. 8b) may be realistic.

510	Despite these uncertainties, our study reveals strong impacts of aerosol DFE on land
511	carbon uptake in China. Although aerosol DFE widely promotes NPP during clear days, NPP
512	shows strongly spatially contrasting responses under all-sky conditions. Aerosol pollution
513	increases NPP by 2-6% in the Northeast where both cloud coverage and particle loading is
514	moderate. Aerosol decreases NPP by 2-4% in both the North China Plain and the Southwest.
515	For the North China Plain, the NPP inhibition is related to the high local pollution level that
516	is above the AOD_{t2} threshold for carbon uptake. Our estimates show that a 44% reduction in
517	local aerosol AOD would help achieve the maximum benefits for plant productivity in this
518	region. In the Southwest, existing cloud cover is already dense and pollution aerosols inhibit
519	NPP in this region. Reductions of pollution aerosol loading will increase carbon uptake in
520	this region.

521	

522	*Acknowledgements.* X. Yue acknowledges funding support from "Thousand Youth Talents
523	Plan". N. Unger acknowledges funding support from The University of Exeter.

524	
525	

Table 1. Summary of studies about diffuse fertilization effects (DFE).

Period	PFTs [a]	Lat.	Method	Diffusion metrics	Results [b]	Reference
1989-1990	DBF	42°S	Flux Obs.	Cloud	NEP is greater on cloudy days than clear days	Hollinger et al. (1994)
1997	Trees	> 53°N	Flux Obs.	Cloud	NEP is greater on cloudy days than clear days	Law et al. (2002)
1998-2000	ENF	40°N	Flux Obs.	Cloud	Maximum NEP is 11% higher on cloudy days than clear days	Monson et al. (2002)
1999-2001	DBF	46°N	Flux Obs.	Cloud	GPP is greater under partly cloudy than clear skies but is reduced under heavy cloud cover.	Rocha et al. (2004)
2002	ENF	39°N	Flux Obs.	Cloud	Mean NEP is 7% greater in cloudy than clear days	Misson et al. (2005)
2001-2013	Varied	35-46°N	Flux Obs.	Cloud	LUE increases with could optical depth (COD). GPP increases if COD < 6.8 but decreases if not.	Cheng et al. (2016)
1992-1993	DBF	43°N	Model	Cloud	Noontime GPP shows maximum increases of 40% by cloud	Gu et al. (2003)
1998-2002	Varied	36-71°N	Flux Obs.	AOD	NEP increases with aerosol loading for forest and crop, but decreases for grassland.	Niyogi et al. (2004)
2002	ENF	39°N	Flux Obs.	AOD	Afternoon NEP increases by 8% by aerosol	Misson et al. (2005)
1999-2002	EBF	10°S	Flux Obs.	AOD	NEP increases by 29% if AOD = 0.1-1.5	Cirino et al. (2014)
July 15th	ENF	30°N	Model	AOD	(1) NPP increase 30% at AOD = 0.6 for clear days (2) NPP decreases with AOD during cloudy days	Cohan et al. (2002)
1992-1993	DBF	43°N	Flux Obs.	Radiation	Noontime GPP increases by 23% by volcanic aerosols under clear sky	Gu et al. (2003)
1999-2003	Trees	3-61°N	Model	Radiation	GPP falls with decreased insolation	Alton et al. (2007)

1999-2001	DBF	46°N	Flux Obs.	DF	Midday GPP is maximum at DF = 0.57	Rocha et al. (2004)
1992-1999	Varied	1°S-71°N	Flux Obs.	DF	GPP is maximum at DF = 0.4-0.7 for trees and shrubs, and DF = 0.2-0.3 for grass	Alton (2008)
2000-2002	DBF	51°N	Flux Obs.	DF	NEP is maximum at DF = 0.28-0.44	Moffat et al. (2010)
2001-2006	Savanna	12°S	Flux Obs.	DF	GPP decreases with increase of DF	Kanniah et al. (2013)
1999-2002	EBF	10°S	Flux Obs.	DF	NEP is maximum at DF = 0.6	Cirino et al. (2014)
2001-2012	Varied	39-46°N	Flux Obs.	DF	Diffuse PAR explained up to 41% of variation in GPP in croplands and up to 17% in forests	Cheng et al. (2015)
2003-2013	Varied	36-46°N	Flux Obs.	DF	GPP is maximum at DF = 0.4-0.6	Strada et al. (2015)
2002	DBF	51°N	Model	DF	GPP is maximum at DF = 0.45	Knohl and Baldocchi (2008)
2002	DBF	51°N	Model	DF	Maximum GPP enhancement of 18% at DF = 0.4	Mercado et al. (2009)
2007	Herbs	36°N	Flux Obs.	CI [c]	NEP is maximum at CI = 0.37 (DF = 0.78)	Jing et al. (2010)
2003-2006	Trees	23-36°N	Flux Obs.	CI	NEP is maximum at CI = 0.4-0.6 (DF = 0.36-0.73)	Zhang et al. (2010)
2008-2009	Herbs	38°N	Flux Obs.	CI	NEP is maximum at CI = 0.4-0.7 (DF = 0.18-0.73)	Bai et al. (2012)

[a] Plant functional types (PFTs) include evergreen needleleaf forest (ENF), deciduous broadleaf forest (DBF), evergreen broadleaf forest (EBF), trees (mixture of ENF/DBF/EBF and shrub), herbs (grass and crop), and savanna.

[b] Carbon metrics include gross primary productivity (GPP), net primary productivity (NPP), and net ecosystem productivity (NEP).

[c] Clearness index (CI) is converted to diffuse fraction (DF) with DF = 1.45 − 1.81×CI (Alton, 2008).

Table 2. Summary of 60 YIBs-CRM simulations**.**

Simulations	AOD ratio [a]	Sky condition	Simulations	AOD ratio	Sky condition
CLR000	0.0	Clear sky [b]	ALL000	0.0	All sky [c]
CLR001	0.1	Clear sky	ALL001	0.1	All sky
CLR002	0.2	Clear sky	ALL002	0.2	All sky
CLR003	0.3	Clear sky	ALL003	0.3	All sky
CLR004	0.4	Clear sky	ALL004	0.4	All sky
CLR005	0.5	Clear sky	ALL005	0.5	All sky
CLR006	0.6	Clear sky	ALL006	0.6	All sky
CLR007	0.7	Clear sky	ALL007	0.7	All sky
CLR008	0.8	Clear sky	ALL008	0.8	All sky
CLR009	0.9	Clear sky	ALL009	0.9	All sky
CLR010	1.0	Clear sky	ALL010	1.0	All sky
CLR012	1.2	Clear sky	ALL012	1.2	All sky
CLR014	1.4	Clear sky	ALL014	1.4	All sky
CLR016	1.6	Clear sky	ALL016	1.6	All sky
CLR018	1.8	Clear sky	ALL018	1.8	All sky
CLR020	2.0	Clear sky	ALL020	2.0	All sky
CLR025	2.5	Clear sky	ALL025	2.5	All sky
CLR030	3.0	Clear sky	ALL030	3.0	All sky
CLR035	3.5	Clear sky	ALL035	3.5	All sky
CLR040	4.0	Clear sky	ALL040	4.0	All sky
CLR050	5.0	Clear sky	ALL050	5.0	All sky
CLR060	6.0	Clear sky	ALL060	6.0	All sky
CLR070	7.0	Clear sky	ALL070	7.0	All sky
CLR080	8.0	Clear sky	ALL080	8.0	All sky
CLR100	10.0	Clear sky	ALL100	10.0	All sky
CLR120	12.0	Clear sky	ALL120	12.0	All sky
CLR150	15.0	Clear sky	ALL150	15.0	All sky
CLR200	20.0	Clear sky	ALL200	20.0	All sky
CLR250	25.0	Clear sky	ALL250	25.0	All sky
CLR300	30.0	Clear sky	ALL300	30.0	All sky

[a] We amplify or diminish base AOD by a certain ratio for each simulation. The base AOD (Fig. 3a) is derived with the aerosol profiles from ModelE2-YIBs climate model and optical parameters from multiple data sources (Fig. S2).
[b] For clear-sky simulations, cloud cover and liquid water path are set to zero.
[c] For all-sky simulations, cloud cover and liquid water path are adopted from the Clouds and the Earth's Radiant Energy System (CERES) SYN1deg Product.

Reference

Alton, P. B., North, P. R., and Los, S. O.: The impact of diffuse sunlight on canopy light-use efficiency, gross photosynthetic product and net ecosystem exchange in three forest biomes, Global Change Biology, 13, 776-787, doi:10.1111/j.1365-2486.2007.01316.x, 2007.

Alton, P. B.: Reduced carbon sequestration in terrestrial ecosystems under overcast skies compared to clear skies, Agricultural and Forest Meteorology, 148, 1641–1653, doi:10.1016/j.agrformet.2008.05.014, 2008.

Amann, M., Bertok, I., Borken-Kleefeld, J., Cofala, J., Heyes, C., Hoglund-Isaksson, L., Klimont, Z., Nguyen, B., Posch, M., Rafaj, P., Sandler, R., Schopp, W., Wagner, F., and Winiwarter, W.: Cost-effective control of air quality and greenhouse gases in Europe: Modeling and policy applications, Environmental Modelling & Software, 26, 1489-1501, doi:10.1016/j.envsoft.2011.07.012, 2011.

Bai, Y., Wang, J., Zhang, B., Zhang, Z., and Liang, J.: Comparing the impact of cloudiness on carbon dioxide exchange in a grassland and a maize cropland in northwestern China, Ecological Research, 27, 615-623, doi:10.1007/s11284-012-0930-z, 2012.

Ball, J. T., Woodrow, I. E., and Berry, J. A.: A model predicting stomatal conductance and its contribution to the control of photosyn- thesis under different environmental conditions, in: Progress in Photosynthesis Research, edited by: Biggins, J., Nijhoff, Dordrecht, Netherlands, 110–112, 1987.

Cheng, S. J., Bohrer, G., Steiner, A. L., Hollinger, D. Y., Suyker, A., Phillips, R. P., and Nadelhoffer, K. J.: Variations in the influence of diffuse light on gross primary productivity in temperate ecosystems, Agricultural and Forest Meteorology, 201, 98-110s, doi:10.1016/j.agrformet.2014.11.002, 2015.

Cheng, S. J., Steiner, A. L., Hollinger, D. Y., Bohrer, G., and Nadelhoffer, K. J.: Using satellite-derived optical thickness to assess the influence of clouds on terrestrial carbon uptake, Journal of Geophysical Research, 121, 1747-1761, doi:10.1002/2016jg003365, 2016.

Cirino, G. G., Souza, R. A. F., Adams, D. K., and Artaxo, P.: The effect of atmospheric aerosol particles and clouds on net ecosystem exchange in the Amazon, Atmospheric Chemistry and Physics, 14, 6523-6543, doi:10.5194/acp-14-6523-2014, 2014.

Clark, D. B., Mercado, L. M., Sitch, S., Jones, C. D., Gedney, N., Best, M. J., Pryor, M., Rooney, G. G., Essery, R. L. H., Blyth, E., Boucher, O., Harding, R. J., Huntingford, C., and Cox, P. M.: The Joint UK Land Environment Simulator (JULES), model description - Part 2: Carbon fluxes and vegetation dynamics, Geoscientific Model Development, 4, 701-722, doi:10.5194/Gmd-4-701-2011, 2011.

Cohan, D. S., Xu, J., Greenwald, R., Bergin, M. H., and Chameides, W. L.: Impact of atmospheric aerosol light scattering and absorption on terrestrial net primary productivity, Global Biogeochemical Cycles, 16, 1090, doi:10.1029/2001gb001441, 2002.

Collins, W. J., Bellouin, N., Doutriaux-Boucher, M., Gedney, N., Halloran, P., Hinton, T., Hughes, J., Jones, C. D., Joshi, M., Liddicoat, S., Martin, G., O'Connor, F., Rae, J., Senior, C., Sitch, S., Totterdell, I., Wiltshire, A., and Woodward, S.: Development and evaluation of an Earth-System model-HadGEM2, Geoscientific Model Development, 4, 1051-1075, doi:10.5194/gmd-4-1051-2011, 2011.

Defries, R. S., Hansen, M. C., Townshend, J. R. G., Janetos, A. C., and Loveland, T. R.: A new global 1-km dataset of percentage tree cover derived from remote sensing, Global Change Biology, 6, 247-254, doi:10.1046/J.1365-2486.2000.00296.X, 2000.

Farquhar, G. D., Caemmerer, S. V., and Berry, J. A.: A Biochemical-Model of Photosynthetic Co2 Assimilation in Leaves of C-3 Species, Planta, 149, 78-90, doi:10.1007/Bf00386231, 1980.

Fu, Q., and Liou, K. N.: Parameterization of the Radiative Properties of Cirrus Clouds, Journal of Atmospheric Sciences, 50, 2008-2025, 1993.

Giorgi, F., Coppola, E., Solmon, F., Mariotti, L., Sylla, M. B., Bi, X., Elguindi, N., Diro, G. T., Nair, V., Giuliani, G., Turuncoglu, U. U., Cozzini, S., Guttler, I., O'Brien, T. A., Tawfik, A. B., Shalaby, A., Zakey, A. S., Steiner, A. L., Stordal, F., Sloan, L. C., and Brankovic, C.: RegCM4: model description and preliminary tests over multiple CORDEX domains, Climate Research, 52, 7-29, doi:10.3354/cr01018, 2012.

Gu, L. H., Baldocchi, D. D., Wofsy, S. C., Munger, J. W., Michalsky, J. J., Urbanski, S. P., and Boden, T. A.: Response of a deciduous forest to the Mount Pinatubo eruption: Enhanced photosynthesis, Science, 299, 2035-2038, doi:10.1126/science.1078366, 2003.

Guo, S., Hu, M., Zamora, M. L., Peng, J., Shang, D., Zheng, J., Du, Z., Wu, Z., Shao, M., Zeng, L., Molina, M. J., and Zhang, R.: Elucidating severe urban haze formation in China, Proceedings of the National Academy of Sciences of the United States of America, 111, 17373-17378, 2014.

Hansen, M. C., DeFries, R. S., Townshend, J. R. G., Carroll, M., Dimiceli, C., and Sohlberg, R. A.: Global Percent Tree Cover at a Spatial Resolution of 500 Meters: First Results of the MODIS Vegetation Continuous Fields Algorithm, Earth Interactions, 7, 1-15, doi:10.1175/1087-3562(2003)007<0001:GPTCAA>2.0.CO;2, 2003.

He, M. Z., Ju, W. M., Zhou, Y. L., Chen, J. M., He, H. L., Wang, S. Q., Wang, H. M., Guan, D. X., Yan, J. H., Li, Y. N., Hao, Y. B., and Zhao, F. H.: Development of a two-leaf light use efficiency model for improving the calculation of terrestrial gross primary productivity, Agricultural and Forest Meteorology, 173, 28-39, doi:Doi 10.1016/J.Agrformet.2013.01.003, 2013.

Hollinger, D. Y., Kelliher, F. M., Byers, J. N., and Hunt, J. E.: Carbon dioxide exchange between an undisturbed old-growth temperate forest and the atmosphere, Ecology, 75, 134-150, 1994.

Jing, X., Huang, J., Wang, G., Higuchi, K., Bi, J., Sun, Y., Yu, H., and Wang, T.: The effects of clouds and aerosols on net ecosystem CO_2 exchange over semi-arid Loess Plateau of Northwest China, Atmospheric Chemistry and Physics, 10, 8205-8218, doi:10.5194/acp-10-8205-2010, 2010.

Jung, M., Reichstein, M., and Bondeau, A.: Towards global empirical upscaling of FLUXNET eddy covariance observations: validation of a model tree ensemble approach using a biosphere model, Biogeosciences, 6, 2001-2013, doi:10.5194/bg-6-2001-2009, 2009.

Kanniah, K. D., Beringer, J., North, P., and Hutley, L.: Control of atmospheric particles on diffuse radiation and terrestrial plant productivity: A review, Progress in Physical Geography, 36, 209-237, doi:10.1177/0309133311434244, 2012.

Kanniah, K. D., Beringer, J., and Hutley, L.: Exploring the link between clouds, radiation, and canopy productivity of tropical savannas, Agricultural and Forest Meteorology, 182-183, 304-313, doi:10.1016/j.agrformet.2013.06.010, 2013.

Knohl, A., and Baldocchi, D. D.: Effects of diffuse radiation on canopy gas exchange processes in a forest ecosystem, Journal of Geophysical Research, 113, G02023, doi:10.1029/2007JG000663, 2008.

Law, B. E., Falge, E., Gu, L., Baldocchi, D. D., Bakwin, P., Berbigier, P., Davis, K., Dolman, A. J., Falk, M., Fuentes, J. D., Goldstein, A., Granier, A., Grelle, A., Hollinger, D., Janssens, I. A., Jarvis, P., Jensen, N. O., Katul, G., Mahli, Y., Matteucci, G., Meyers, T., Monson, R., Munger, W., Oechel, W., Olson, R., Pilegaard, K., Paw, K. T., Thorgeirsson, H., Valentini, R., Verma, S., Vesala, T., Wilson, K., and Wofsy, S.: Environmental controls over carbon dioxide and water vapor exchange of terrestrial vegetation,

Agricultural and Forest Meteorology, 113, 97-120, doi:10.1016/S0168-1923(02)00104-1, 2002.

Li, T., Heuvelink, E., Dueck, T. A., Janse, J., Gort, G., and Marcelis, L. F. M.: Enhancement of crop photosynthesis by diffuse light: quantifying the contributing factors, Annales of Botany, 114, 145-156, 2014.

Liu, Z., Guan, D. B., Wei, W., Davis, S. J., Ciais, P., Bai, J., Peng, S. S., Zhang, Q., Hubacek, K., Marland, G., Andres, R. J., Crawford-Brown, D., Lin, J. T., Zhao, H. Y., Hong, C. P., Boden, T. A., Feng, K. S., Peters, G. P., Xi, F. M., Liu, J. G., Li, Y., Zhao, Y., Zeng, N., and He, K. B.: Reduced carbon emission estimates from fossil fuel combustion and cement production in China, Nature, 524, 335-338, doi:10.1038/nature14677, 2015.

Mercado, L. M., Bellouin, N., Sitch, S., Boucher, O., Huntingford, C., Wild, M., and Cox, P. M.: Impact of changes in diffuse radiation on the global land carbon sink, Nature, 458, 1014-U1087, doi:10.1038/Nature07949, 2009.

Misson, L., Lunden, M., McKay, M., and Goldsteina, A. H.: Atmospheric aerosol light scattering and surface wetness influence the diurnal pattern of net ecosystem exchange in a semi-arid ponderosa pine plantation, Agricultural and Forest Meteorology, 129, 69-83, 2005.

Moffat, A. M., Beckstein, C., Churkina, G., Mund, M., and Heimann, M.: Characterization of ecosystem responses to climatic controls using artificial neural networks, Global Change Biology, 16, 2737-2749, doi:10.1111/J.1365-2486.2010.02171.X, 2010.

Monfreda, C., Ramankutty, N., and Foley, J. A.: Farming the planet: 2. Geographic distribution of crop areas, yields, physiological types, and net primary production in the year 2000, Global Biogeochemical Cycles, 22, Gb1022, doi:10.1029/2007gb002947, 2008.

Monson, R. K., Turnipseed, A. A., Sparks, J. P., Harley, P. C., Scott-Denton, L. E., Sparks, K., and uxman, T. E.: Carbon sequestration in a high-elevation, subalpine forest, Global Change Biology, 8, 459-478, doi:10.1046/j.1365-2486.2002.00480.x, 2002.

Niyogi, D., Chang, H.-I., Saxena, V. K., Holt, T., Alapaty, K., Booker, F., Chen, F., Davis, K. J., Holben, B., Matsui, T., Meyers, T., Oechel, W. C., Sr., R. A. P., Wells, R., Wilson, K., and Xue, Y.: Direct observations of the effects of aerosol loading on net ecosystem CO_2 exchanges over different landscapes, Geophysical Research Letters, 31, doi:10.1029/2004GL020915, 2004.

Oliphant, A. J., Dragoni, D., Deng, B., Grimmond, C. S. B., Schmid, H. P., and Scott, S. L.: The role of sky conditions on gross primary production in a mixed deciduous forest, Agricultural and Forest Meteorology, 151, 781-791, doi:10.1016/J.Agrformet.2011.01.005, 2011.

Pan, Y., Birdsey, R., Hom, J., McCullough, K., and Clark, K.: Improved estimates of net primary productivity from MODIS satellite data at regional and local scales, Ecological Applications, 16, 125-132, doi:10.1890/05-0247, 2006.

Pavlick, R., Drewry, D. T., Bohn, K., Reu, B., and Kleidon, A.: The Jena Diversity-Dynamic Global Vegetation Model (JeDi-DGVM): a diverse approach to representing terrestrial biogeography and biogeochemistry based on plant functional trade-offs, Biogeosciences, 10, 4137-4177, doi:10.5194/bg-10-4137-2013, 2013.

Piao, S. L., Fang, J. Y., Ciais, P., Peylin, P., Huang, Y., Sitch, S., and Wang, T.: The carbon balance of terrestrial ecosystems in China, Nature, 458, 1009-1013, doi:10.1038/nature07944, 2009.

Rap, A., Spracklen, D. V., Mercado, L., Reddington, C. L., Haywood, J. M., Ellis, R. J., Phillips, O. L., Artaxo, P., Bonal, D., Coupe, N. R., and Butt, N.: Fires increase Amazon forest productivity through increases in diffuse radiation, Geophysical Research Letters, 42, 4654-4662, doi:10.1002/2015gl063719, 2015.

Rasch, P. J., Mahowald, N. M., and Eaton, B. E.: Representations of transport, convection, and the hydrologic cycle in chemical transport models: Implications for the modeling of short-lived and soluble species, Journal of Geophysical Research, 102, 28127–28138, doi:10.1029/97JD02087, 1997.

Remer, L. A., Kaufman, Y. J., Tanré, D., Mattoo, S., Chu, D. A., Martins, J. V., Li, R.-R., Ichoku, C., Levy, R. C., Kleidman, R. G., Eck, T. F., Vermote, E., and Holben, B. N.: The MODIS Aerosol Algorithm, Products, and Validation, Journal of Atmospheric Sciences, 62, 947-973, 2005.

Rocha, A. V., Su, H. B., Vogel, C. S., Schmid, H. P., and Curtis, P. S.: Photosynthetic and water use efficiency responses to diffuse radiation by an aspen-dominated northern hardwood forest, Forest Science, 50, 793-801, 2004.

Rutan, D. A., Kato, S., Doelling, D. R., Rose, F. G., Nguyen, L. T., Caldwell, T. E., and Loeb, N. G.: CERES Synoptic Product: Methodology and Validation of Surface Radiant Flux, Journal of Atmospheric and Oceanic Technology, 32, 1121-1143, doi:10.1175/JTECH-D-14-00165.1, 2015.

Schmidt, G. A., Kelley, M., Nazarenko, L., Ruedy, R., Russell, G. L., Aleinov, I., Bauer, M., Bauer, S. E., Bhat, M. K., Bleck, R., Canuto, V., Chen, Y. H., Cheng, Y., Clune, T. L., Del Genio, A., de Fainchtein, R., Faluvegi, G., Hansen, J. E., Healy, R. J., Kiang, N. Y., Koch, D., Lacis, A. A., LeGrande, A. N., Lerner, J., Lo, K. K., Matthews, E. E., Menon, S., Miller, R. L., Oinas, V., Oloso, A. O., Perlwitz, J. P., Puma, M. J., Putman, W. M., Rind, D., Romanou, A., Sato, M., Shindell, D. T., Sun, S., Syed, R. A., Tausnev, N., Tsigaridis, K., Unger, N., Voulgarakis, A., Yao, M. S., and Zhang, J. L.: Configuration and assessment of the GISS ModelE2 contributions to the CMIP5 archive, Journal of Advances in Modeling Earth Systems, 6, 141-184, doi:10.1002/2013ms000265, 2014.

Spitters, C. J. T.: Separating the Diffuse and Direct Component of Global Radiation and Its Implications for Modeling Canopy Photosynthesis .2. Calculation of Canopy Photosynthesis, Agricultural and Forest Meteorology, 38, 231-242, doi:10.1016/0168-1923(86)90061-4, 1986.

Still, C. J., Riley, W. J., Biraud, S. C., Noone, D. C., Buenning, N. H., Randerson, J. T., Torn, M. S., Welker, J., White, J. W. C., Vachon, R., Farquhar, G. D., and Berry, J. A.: Influence of clouds and diffuse radiation on ecosystem-atmosphere CO2 and (COO)-O-18 exchanges, J. Geophys. Res., 114, G01018, doi:10.1029/2007jg000675, 2009.

Strada, S., Unger, N., and Yue, X.: Observed aerosol-induced radiative effect on plant productivity in the eastern United States, Atmos. Environ., 122, 463–476, doi:10.1016/j.atmosenv.2015.09.051, 2015.

Tian, H. Q., Melillo, J., Lu, C. Q., Kicklighter, D., Liu, M. L., Ren, W., Xu, X. F., Chen, G. S., Zhang, C., Pan, S. F., Liu, J. Y., and Running, S.: China's terrestrial carbon balance: Contributions from multiple global change factors, Global Biogeochemical Cycles, 25, Gb1007, doi:10.1029/2010gb003838, 2011.

Wang, H. J., and Chen, H. P.: Understanding the recent trend of haze pollution in eastern China: roles of climate change, Atmos. Chem. Phys., 16, 4205-4211, doi:10.5194/acp-16-4205-2016, 2016.

Wielicki, B. A., Barkstrom, B. R., Harrison, E. F., Lee, R. B., Smith, G. L., and Cooper, J. E.: Clouds and the earth's radiant energy system (CERES): An earth observing system experiment, Bulletin of the American Meteorological Society, 77, 853-868, doi:10.1175/1520-0477(1996)077<0853:Catere>2.0.Co;2, 1996.

Xia, X.: A closer looking at dimming and brightening in China during 1961-2005, Annales Geophysicae, 28, 1121-1132, doi:10.5194/angeo-28-1121-2010, 2010.

Xiao, J. F., Zhou, Y., and Zhang, L.: Contributions of natural and human factors to increases in vegetation productivity in China, Ecosphere, 6, 233, doi:10.1890/Es14-00394.1, 2015.

Yue, X., Wang, H., Liao, H., and Fan, K.: Simulation of dust aerosol radiative feedback using the GMOD: 2. Dust-climate interactions, J. Geophys. Res., 115, D04201, doi:10.1029/2009JD012063, 2010.

Yue, X., and Liao, H.: Climatic responses to the shortwave and longwave direct radiative effects of sea salt aerosol in present day and the last glacial maximum, Clim. Dyn., 39, 3019-3040, doi:10.1007/S00382-012-1312-5, 2012.

Yue, X., and Unger, N.: The Yale Interactive terrestrial Biosphere model version 1.0: description, evaluation and implementation into NASA GISS ModelE2, Geosci. Model Dev., 8, 2399-2417, doi:10.5194/gmd-8-2399-2015, 2015.

Yue, X., Unger, N., Keenan, T. F., Zhang, X., and Vogel, C. S.: Probing the past 30-year phenology trend of U.S. deciduous forests, Biogeosciences, 12, 4693-4709, doi:10.5194/bg-12-4693-2015, 2015a.

Yue, X., Unger, N., and Zheng, Y.: Distinguishing the drivers of trends in land carbon fluxes and biogenic emissions over the past three decades, Atmos. Chem. Phys., 15, 11931-11948, doi:10.5194/acp-15-11931-2015, 2015b.

Zhang, M., Yu, G. R., Zhang, L. M., Sun, X. M., Wen, X. F., Han, S. J., and Yan, J. H.: Impact of cloudiness on net ecosystem exchange of carbon dioxide in different types of forest ecosystems in China., Biogeosciences, 7, 711-722, doi:10.5194/bg-7-711-2010, 2010.

Zhao, M. S., Heinsch, F. A., Nemani, R. R., and Running, S. W.: Improvements of the MODIS terrestrial gross and net primary production global data set, Remote Sensing of Environment, 95, 164-176, doi:10.1016/J.Rse.2004.12.011, 2005.
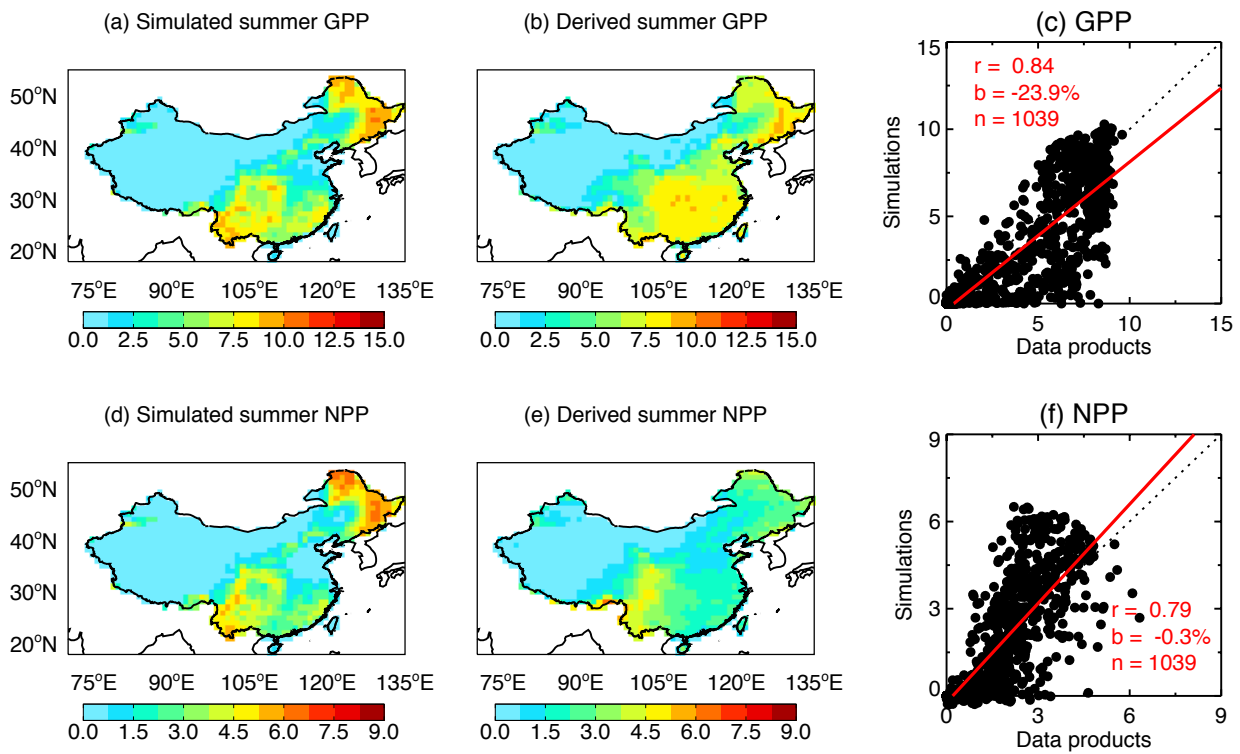
Figure 1. Evaluation of summertime carbon fluxes simulated with the YIBs model. Simulations are (a) GPP and (d) NPP from ALL010. Derived carbon fluxes are averaged for 2009-2011, with (b) GPP from the benchmark upscaling of flux tower data and (e) NPP from MODIS. The aerosol DFE is included in the simulation. The correlation coefficients (r), relative biases (b), and number of 1°×1° grid cells (n) for the comparisons are listed on the scatter plots (c and f). The dashed line represents the 1:1 ratio. The red line is the linear regression between simulations (predictand) and data products (predictor). Units of GPP and NPP is g C m^{-2} day^{-1}.
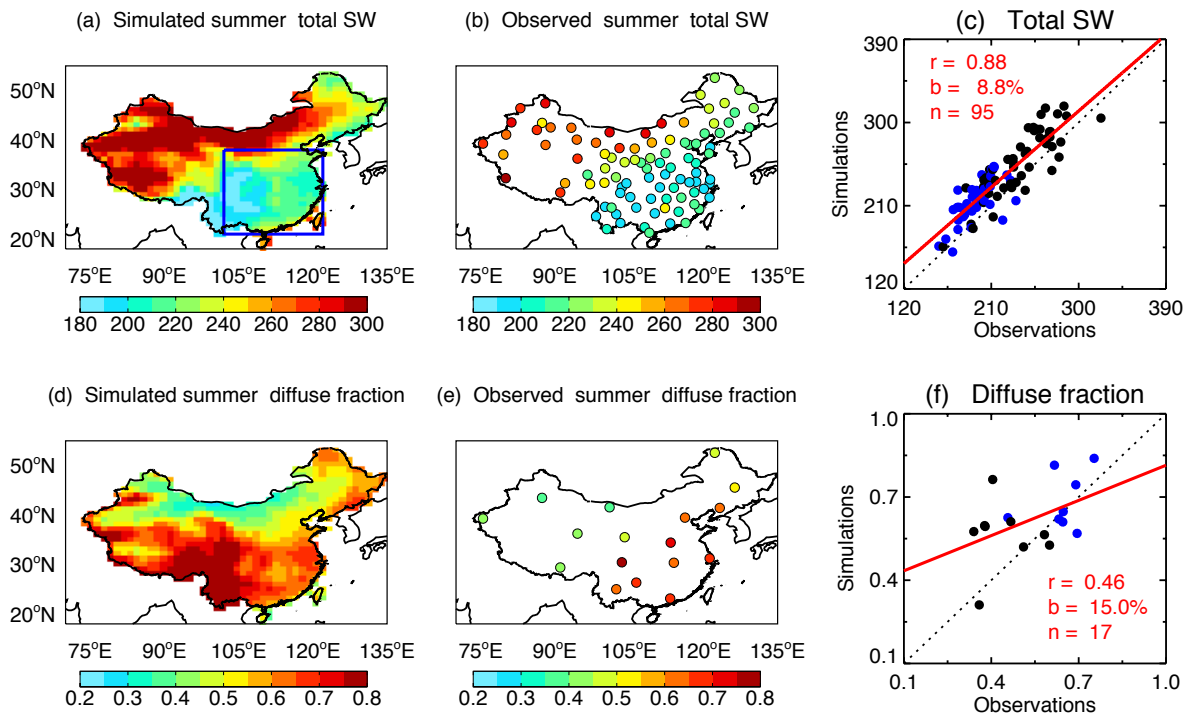
Figure 2. Evaluation of summertime radiation fluxes simulated with the CRM model. Simulations are (a) surface total shortwave radiation (W m^{-2}) and (d) diffuse radiation fraction from ALL010 with 1°×1° resolution. Observations (b and e) are the average during 2008-2012 from 106 sites operated by the Climate Data Center, Chinese Meteorological Administration. The correlation coefficients (r), relative biases (b), and number of sites (n) are shown in the scatter plots (c and f). The blue points in the scatter plots represent sites located within the box regions in eastern China as shown in (a). The dashed line represents the 1:1 ratio. The red line is the linear regression between simulations and observations.
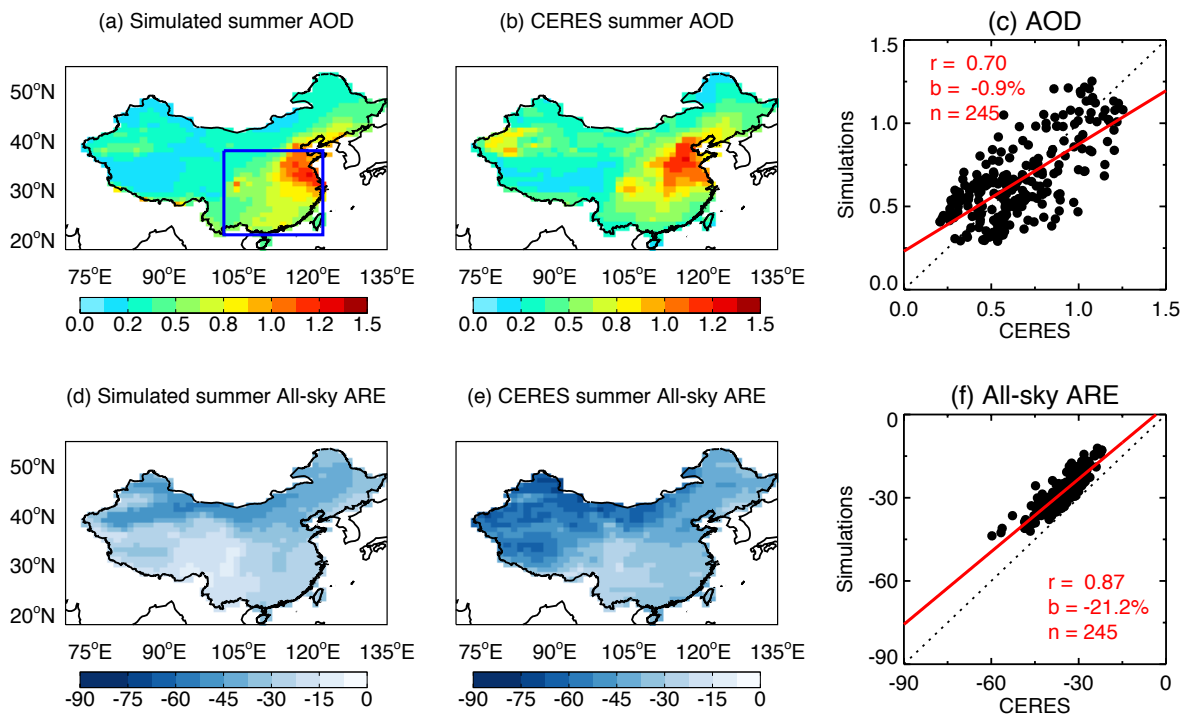
Figure 3. Evaluation of aerosol radiative effects simulated with the CRM model. Panels show the simulated (a) AOD at 550 nm and (d) all-sky aerosol radiative efficiency (ARE, W m^{-2} per unit AOD) with that from the CERES SYN1deg product (b, e). The correlation coefficients (r), relative biases (b), and number of 1°×1° grid cells (n) for the comparisons over the box domain in figure (a) are listed on the scatter plots (c, f). The dashed line represents the 1:1 ratio. The red line is the linear regression between simulations and data products.
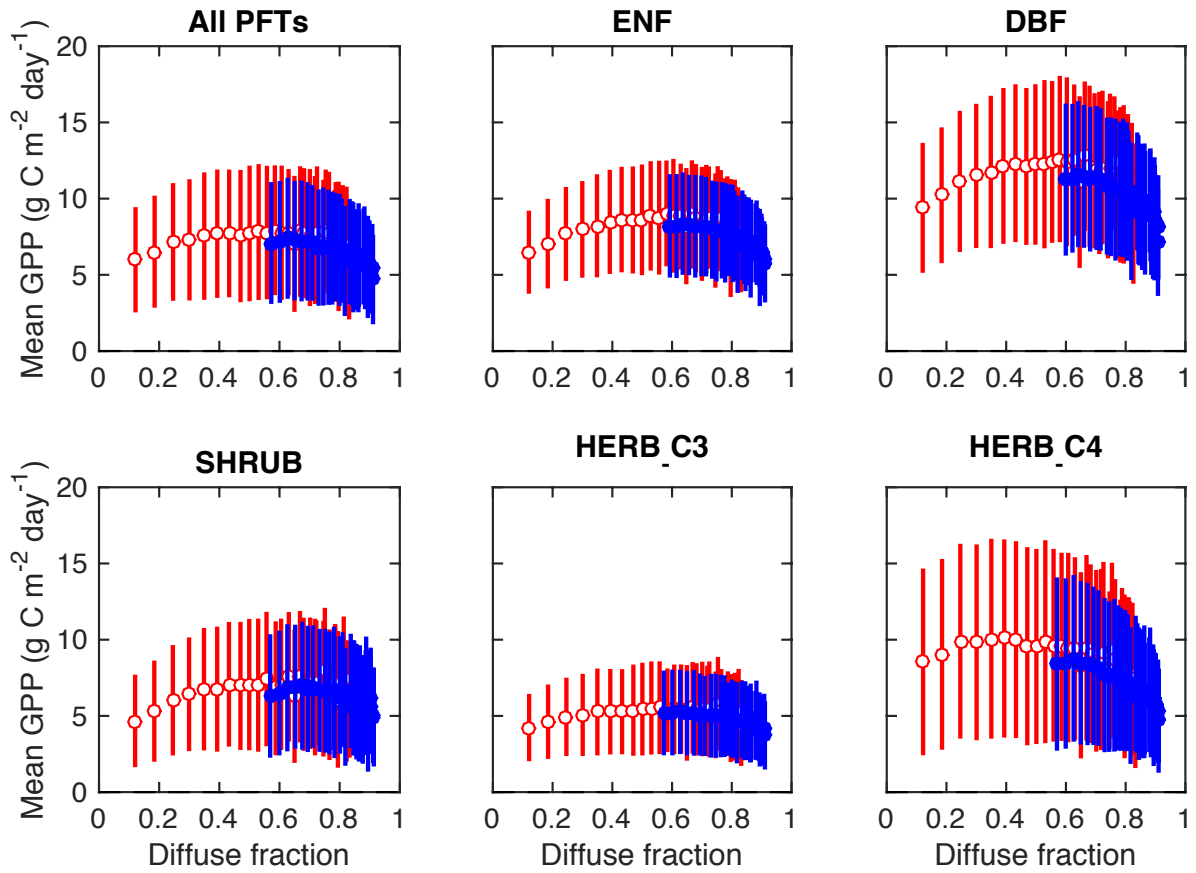
Figure 4. Mean summer GPP for different diffuse fractions. Results shown are for clear-sky (red empty points) and all-sky (blue solid points) conditions. Separately for clear-sky and all-sky conditions, we first collect all grid cells in eastern China (box region in Fig. 2a) for all 30 sensitivity simulations. We then aggregate all grid cells with non-zero fraction of a specific PFT into 30 AOD bins ranging from 0 to 6 at an interval of 0.2. In each bin, we calculate average diffuse fraction and corresponding GPP, with an error bar indicating one standard deviation.
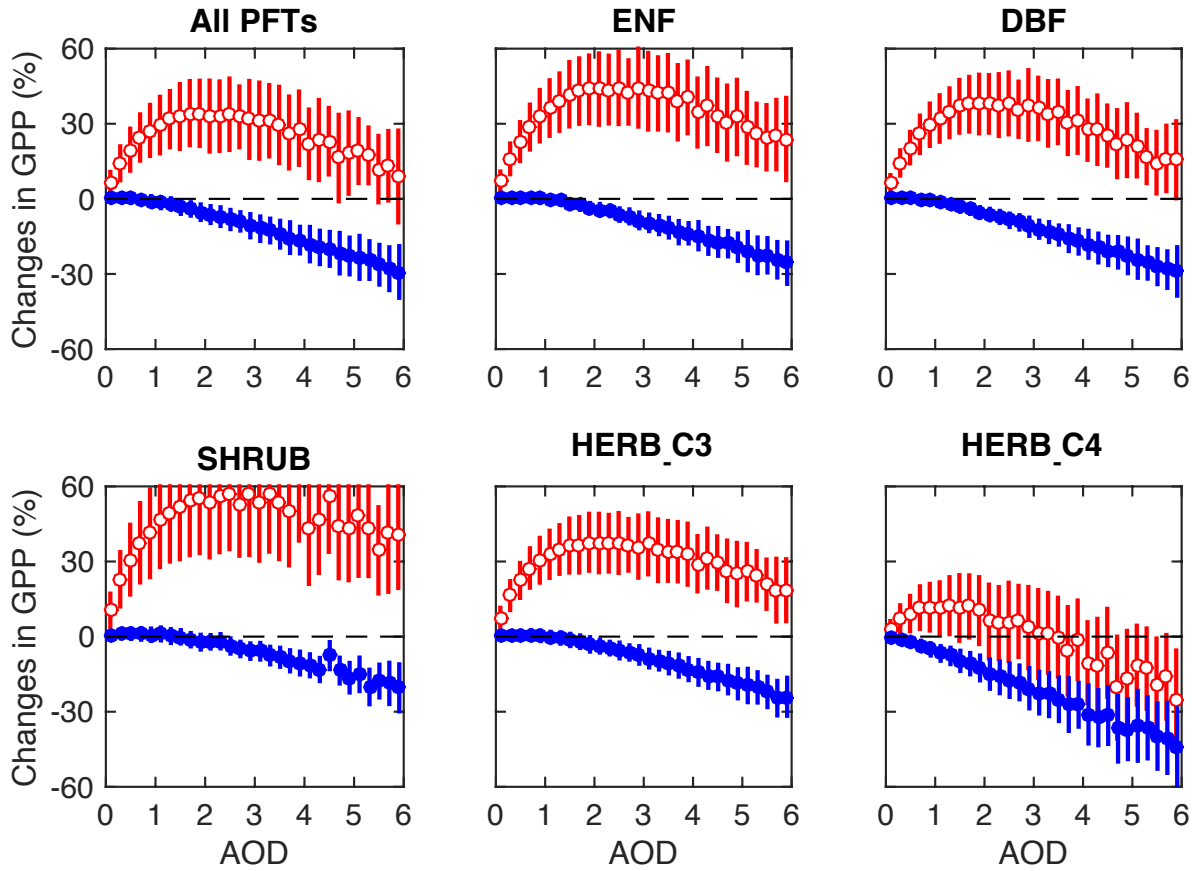
Figure 5. Sensitivity of summer GPP to changes of AOD. Results shown are different for clear-sky (red empty points) and all-sky (blue solid points) conditions in summer (June-August). Separately for clear-sky and all-sky conditions, we first collect all grid cells in eastern China (box region in Fig. 2a) for all 30 sensitivity simulations (Table 2). We then aggregate all grid cells with non-zero fraction of the specific PFT into 30 AOD bins ranging from 0 to 6 at an interval of 0.2. In each bin, we calculate average GPP change relative to aerosol-free conditions, with an error bar indicating one standard deviation.
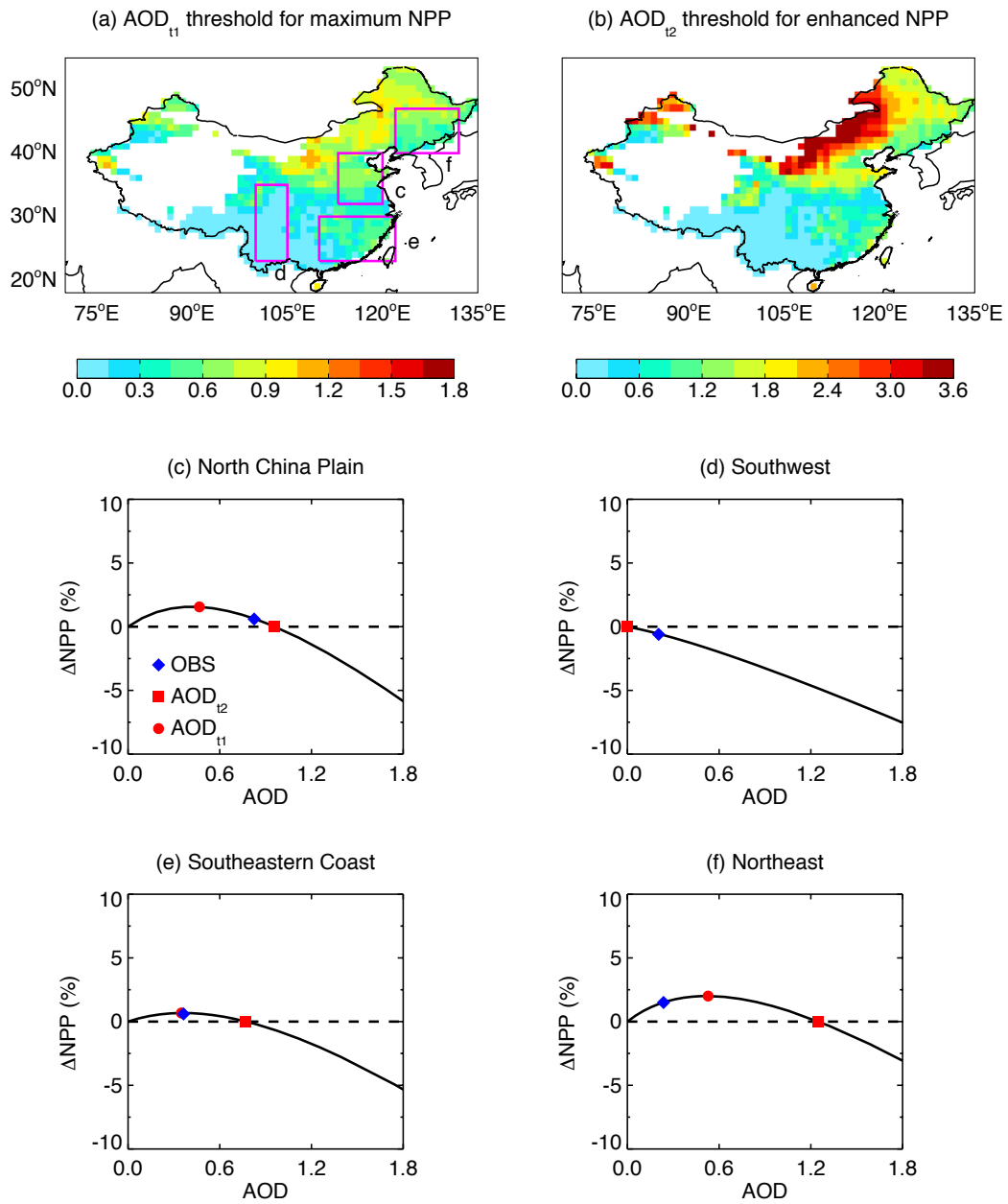
Figure 6. Thresholds of AOD at 550 nm for aerosol DFE. (a) AOD_{t1} threshold leading to maximum NPP in summer (June-August). (b) AOD_{t2} threshold leading to enhanced summer NPP. Aerosol indirect effects and climatic feedback are not included for these thresholds. The average AOD-NPP response curves at four box domains in (a) are shown in (c-f), with red symbols indicating two AOD thresholds and blue symbols indicating observed AOD from MODIS. Chinese regions with low aerosol-free NPP (<0.05 g C m^{-2} day^{-1}) are blanked in (a-b). Color scales for (a) and (b) are different.
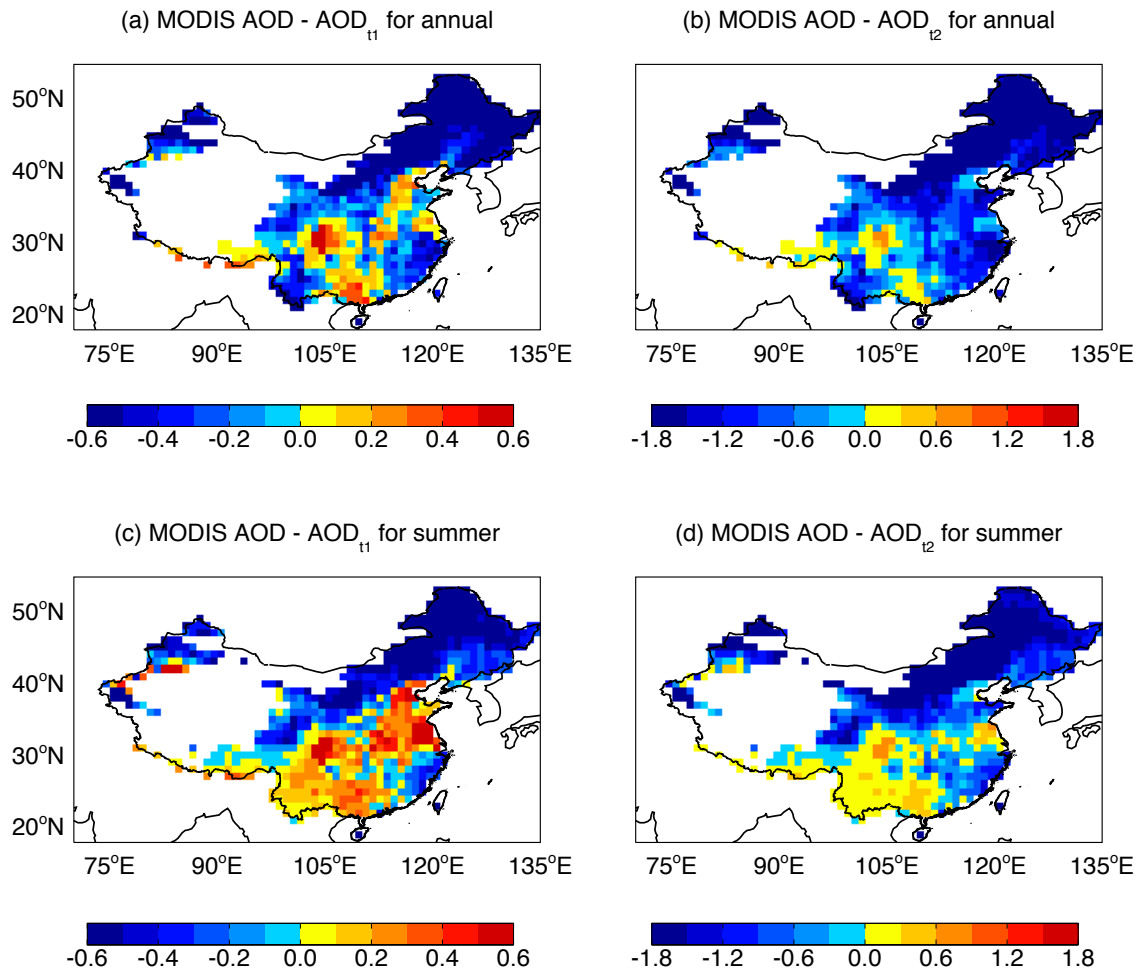
Figure 7. Differences between MODIS AOD and two derived AOD thresholds. Left panel shows ΔAOD between MODIS and AOD_{t1} for the average of (a) whole year and (c) summer months. Right panel shows ΔAOD between MODIS and AOD_{t2} for the average of (b) whole year and (d) summer months. For the left panel, regions with positive values indicate that increase (decrease) of local AOD leads to reductions (enhancement) in NPP, while regions with negative values denote that decrease (increase) of local AOD results in reductions (enhancement) in NPP. For the right panel, regions with negative (positive) values indicate that current level of AOD always promotes (inhibits) NPP, compared with the aerosol-free conditions. The color scales among panels are different.
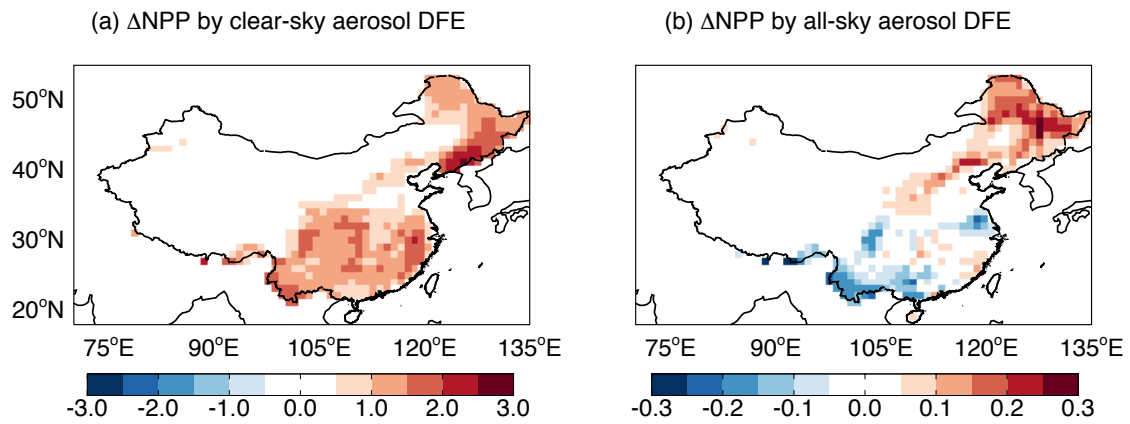
Figure 8. Changes in summer NPP caused by aerosol DFE in China for (a) clear-sky (CLR010 – CLR000) and (b) all-sky (ALL010 – ALL000) conditions. The percentage changes of NPP are shown in Figure S7. The color scales between panels are different. Units: g C m^{-2} day^{-1}.